INSTITUTE OF PHYSICS PUBLISHING JOURNAL OF PHYSICS D: APPLIED PHYSICS

J. Phys. D: Appl. Phys. **37** (2004) 3266–3276 PII: S0022-3727(04)84475-9

EUV discharge light source based on a dense plasma focus operated with positive and negative polarity

I V Fomenkov, N Böwering, C L Rettig, S T Melnychuk, I R Oliver, J R Hoffman, O V Khodykin, R M Ness and W N Partlo

Cymer Inc., 17075 Thormint Ct, San Diego, CA 92127, USA

Received 29 July 2004, in final form 15 October 2004
Published 19 November 2004
Online at stacks.iop.org/JPhysD/37/3266
doi:10.1088/0022-3727/37/23/007

Abstract

The application of a dense plasma focus pinch discharge as a light source for extreme ultraviolet (EUV) lithography is discussed. For operation with xenon gas, the radiation emitted at around 13.5 nm is analysed with temporal, spectral or spatial resolution. We describe and compare the operating characteristics and plasma dynamics of the device when energized at positive and negative polarity of the charging voltage. The thermal load distribution, heat deposition and wear of the electrodes are measured and compared for both configurations. High-repetition rate burst mode data show characteristic transients. Source size data are also obtained when tin powder is used as the target element. More favourable performance characteristics were generally obtained for operation of the pinch discharge at negative polarity.

(Some figures in this article are in colour only in the electronic version)

1. Introduction

Lithography at extreme ultraviolet (EUV) wavelengths has been chosen by the semiconductor industry as the main contender for future chip manufacturing at the 32 nm node and beyond. Significant research and development efforts have already been devoted to this technology during the last five years. The EUV programme is presently gaining momentum; critical challenges and technology hurdles in key areas are actively addressed and solved to meet the aggressive road maps that are in place to reach high-volume manufacturing with EUV exposure tools at the end of this decade. A pulsed plasma light source with extremely high power and brightness is required for integration into a stepper tool based on all-reflective optics with multilayer (ML) coatings. The mirror reflectance at normal incidence is only ∼70% for each surface; thus only a small fraction of the radiation produced will reach the wafer. Therefore, to achieve high production throughput, the EUV source power has to be in the range of 80–120 W within a bandwidth of 2% at the wavelength of choice, 13.5 nm, with high spectral purity. Repetition frequencies of more than 6000 Hz and integrated (50-pulse) energy stabilities of ±0.3% are needed to meet the dose requirements of the scanner tool. Furthermore, the demand for brightness leads to a source etendue in the range of 1–3.3 mm^2 sr with a maximum input solid angle to the illuminator section of 0.2 sr. Source cleanliness is also very important and translates to a lifetime requirement of more than 30 000 h. At Cymer, we have chosen a dense plasma focus (DPF) configuration for development efforts devoted to a discharge-produced plasma (DPP) source targeted for EUV technology.

The plasma focus concept was initiated long ago by the pioneering work of Filippov *et al* [1] and Mather [2]. Apart from the main application of large-scale DPF devices in fusion research, small-energy down-scaled instruments (with less than ∼1 kJ stored energy) were also investigated in the past by several groups and operated at higher repetition frequencies to serve as intense radiation sources [3–9]. In addition, the application of a DPF to proximity x-ray and soft x-ray lithography was discussed [10–15]. Our choice of source configuration was born out of past development work on coaxial plasma guns and plasma thrusters for space

applications [16–20]. By employing pulse energies in the range of only 10–20 J the scaling to the required repetition rates of several kilohertz can be accomplished with reliable all-solid-state pulsed power drivers and advanced thermal management of water-cooled electrodes. Compared with our earlier-generation test devices [21, 22], the present DPF configuration produces significantly higher plasma temperatures due to its shorter pulse length and higher output voltage, leading to a higher discharge peak current with faster rise time.

In accordance with traditional practice we have initially operated our DPF discharge with positive polarity, i.e. the central electrode was the anode. Commonly, it is observed that the neutron or x-ray yield for a DPF is several orders of magnitude higher with a positive inner electrode. However, this behaviour, also termed the 'polarity riddle of the plasma focus' [23], can be strongly influenced by the radial electric field during sheath build-up, and successful operation of negative polarity machines has also been described [23–27]. In particular, this mode of operation had considerable benefits in terms of electrode heating, erosion and contamination. We have therefore also tested our lithography light source with reversed polarity. For use with positive polarity, many aspects of our radiation source have already been discussed in detail in previous reports [28–31]. The spectral emission characteristics were analysed by comparison with model calculations [32]. Here, we describe the operation of the DPF with negative polarity and compare results obtained with both positive and negative polarity of the inner electrode. In particular, we discuss recent thermal measurements, calorimetry and in-band output data obtained in burst mode at high repetition rates with these configurations. In addition, new results are reported on source size and pulse shape. Furthermore, we describe the results obtained with tin as an alternative target element.

2. Experimental arrangement

2.1. Source configuration and pulsed power waveforms

The main features and the configuration of our DPF apparatus with pulse compression have been described previously [28–31]. Apart from the polarity, the electric power components are the same for negative and positive DPF. Switching the polarity is fairly straightforward. It mainly involves sign reversal of charging power supplies, solid-state elements and bias coils. Figure 1 illustrates the schematics of the coaxial electrode arrangement and the low-inductance pulsed-power compression circuit (for the case of negative polarity). Using reliable solid-state switches (S_1) and magnetic compression switches (LS_1, LS_2), the output from a resonant charger is stepped up by a transformer to about 4.5 kV and then transferred to the output capacitor, C_2. After saturation of the magnetic output switch (LS_3) the stored energy is applied to the load in about 150 ns. The rise time is less than 50 ns and the energy deposited in the discharge is usually at around 10–12 J. As the current starts to flow a sliding discharge is initiated between the electrodes in the case when the anode is the inner electrode. To aid in the breakdown process in this region an independently operated pre-ionization system is triggered about 1 μs earlier. The $J \times B$ force accelerates the plasma sheet towards the end of the electrodes where radial

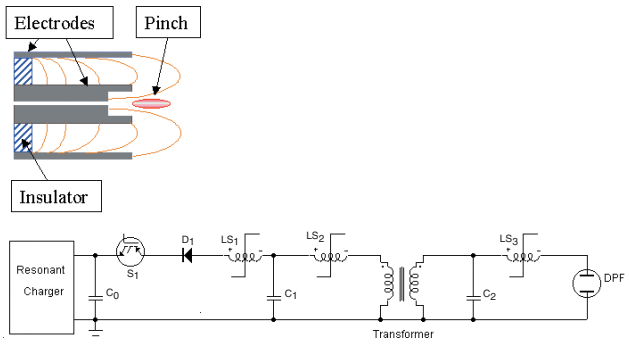

Figure 1. Schematic view of the DPF electrode arrangement and circuit diagram for the pulse charging components using negative polarity.

forces lead to the formation of a dense pinch region. High stages of ionization are reached in this hot plasma zone, and radiation in the EUV region is emitted.

The pinch discharge is usually operated with a xenon/helium mixture. Typically, the total pressure in the discharge chamber is kept constant and the flow rates of xenon and helium are varied. Xenon is injected on-axis and helium is admitted more diffusely at a location further away from the discharge region as described earlier, for example, in [29]. In the pinch region, helium is completely ionized and the EUV radiation produced in the 10–20 nm wavelength region is entirely due to emission from highly ionized xenon [32].

For negative-polarity configurations the breakdown and initial plasma development processes were found to be distinctly different. At some time after the discharge initiation process, a pinch develops in front of the electrodes, as with the positive-polarity configuration. However, the plasma is initiated within the cathode on the symmetry axis. An electron source for pre-ionization is effective in assisting breakdown only if it is applied in this region. Consequently, pre-ionization through hollows of the outer electrode, as in the case of the positive DPF [29, 30], is inefficient. Pre-ionization pins at other locations, in contrast, can lead to discharge initiation of the central hollow region in the cathode, and intense EUV radiation is generated in the subsequent pinch event. However, it was also found that a self-breakdown mode without pre-ionization produces EUV radiation efficiently.

Voltage waveforms are probed at the C_2 capacitor deck and at a location between the saturable inductor LS_3 and the central electrode. Typical voltage waveforms together with the EUV signal for a negative polarity DPF are shown in figure 2. Apart from the sign change, there are several more subtle differences compared with the waveforms observed from a positively charged DPF with pre-ionization [28]. When LS_2 has switched, negative charge begins to arrive at the C_2 capacitors. As the negative voltage, $V(C_2)$, increases, the magnitude of the cathode potential is at first also increasing towards more negative values since there is no discharge at this point in time. Then a breakdown occurs and the magnitude of the cathode voltage decreases sharply to a much smaller value corresponding to the voltage drop across the discharge region. The voltage $V(C_2)$ continues to rise to more negative values while the cathode voltage stays low since current flow is held off by the coil LS_3. At maximum C_2 potential or shortly

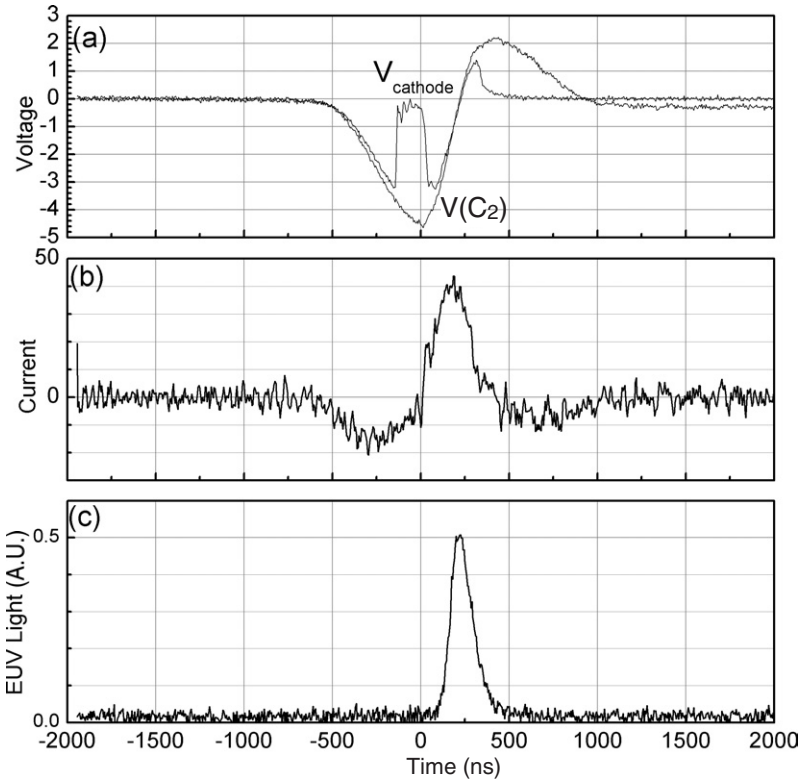

Figure 2. Waveforms versus time (single pulse): (*a*) capacitor voltage, $V(C_2)$, and cathode voltage; (*b*) discharge current as derived from the $V(C_2)$ voltage waveform; (*c*) EUV monitor output (into 4% bandwidth at 13.5 nm). Note that the discharge time is of the order of 100 ns.

thereafter the inductor LS_3 is saturated and switches, resulting in the application of the full voltage across the electrode gap. This is seen from the very fast appearance of a high negative voltage at the cathode probe. As the discharge develops and both voltage waveforms approach the zero value of their half-cycle oscillation, the pinch event occurs and the discharge current (shown in figure 2(*b*)) goes through a maximum. The current was calculated from the C_2 capacitance and the time derivative of the voltage waveform, dV/dt. (Previous measurements with a magnetic B-dot probe on a DPF with positive polarity have confirmed the proportionality of these current signals.) The peak in the current is reflected by the emission of the EUV light pulse (figure 2(*c*)) as detected using the EUV monitor. The following voltage reversal in the waveforms (see figure 2(*a*)) is due to non-dissipated reflected pulse energy and analogous to the positive-polarity case [28]. The characteristic rise and fall times of the EUV pulse are ~20 ns, and the typical pulse duration is ~70 ns (full-width at half-maximum, FWHM).

2.2. *EUV energy detection scheme*

Compared with previously used schemes [28–31], we have designed a more compact EUV energy monitor. Its construction is outlined in figure 3. An oblique Mo/Si ML mirror designed for an incidence angle of 45° and a 0.2 μm thick zirconium foil on a holder with 5 mm diameter aperture are used as filters for the 13.5 nm band in front of a fast uncoated silicon photodiode (IRD-AXUV-G-100). A differentially pumped tube separates the energy monitor from the higher-pressure discharge region. The EUV pulse shown in figure 2

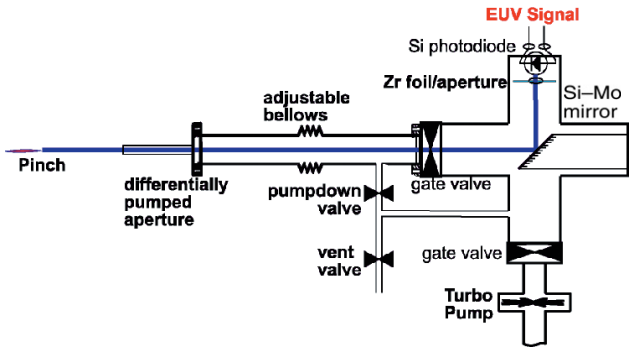

Figure 3. Diagram of compact energy monitor assembly using a 45° ML mirror.

was recorded with an arrangement of this type. The zirconium foil also suppresses visible light. Due to the influence of oxide layers the transmission for 13.5 nm EUV radiation cannot be reliably inferred from the Zr foil thickness alone. Therefore, we have measured the transmission using two Zr foils behind each other and moving the second Zr foil in and out of the EUV beam in this configuration. With the corresponding geometric factor (distance from the pinch to the aperture) and the quantum efficiency of the photodiode the absolute EUV pulse energy can in principle be determined from the signal by integrating the detected change at the photodiode. This method was described earlier in more detail for other intensity monitor arrangements [28]. Since slight reductions by gas absorption and mirror degradation due to debris impact are neglected, this leads to a lower limit on the emitted EUV energy per pulse. In other words, it is safe to conclude that although the data obtained

with the EUV monitor could cause an underestimation of the actual EUV emission intensity and pulse energy, they cannot lead to an overestimation of these values.

2.3. Plasma dynamics for positive and negative polarity

Using visible light CCD cameras with 10 ns gating and imaging with a zoom lens behind a vacuum window, we have also investigated the discharge plasma dynamics for both polarities and several electrode configurations with respect to initial plasma phases, pinch development and decay of the hot plasma zone. Here we give a summary of these observations that outlines the differences observed with respect to polarity. When operated at positive voltage and with pre-ionization, the DPF showed the well-known behaviour with the development of a current sheet in the annular space between the electrodes in a run-down phase. This is followed by a compression phase in the radial direction when the sheet reaches the front of the inner electrode. Electron bombardment occurs at various locations at the front end of the inner electrode. The negative polarity operation (without pre-ionization) gave the best performance when the gas injection aperture and the inner diameter of the inner electrode were fairly large (ca 4 mm). The aspect ratio of length to diameter is within the range typically associated with a hollow cathode breakdown. A different discharge configuration with somewhat similar breakdown characteristics (not a DPF, but also operated with negative polarity), called a hollow-cathode-triggered pinch, has been employed for EUV generation by another group [33].

We have used a gated ultra-fast framing camera to record the plasma development at different times during the discharge pulse. This camera has the advantage that several gated exposures can be made at different times in a *single* pulse. These data illustrate the very different plasma initiation behaviour. Figure 4(*a*) displays a series of visible-light-images of the positive-polarity DPF taken at time intervals of 20 ns during the discharge development. The pinch formation occurs after a run-down phase after more than 60 ns. Some plasma instabilities are observed as well. Figure 4(*b*) shows a corresponding series with similar magnification for the time period before the pinch formation when the discharge is operated with negative polarity at time intervals of 20 ns. It can be clearly seen that the plasma develops first on the axis (see first time frame). Once the plasma near the front end of the electrodes is ignited, radial compression and pinching occur in this region. The ions are moving towards the inner electrode in this configuration. However, an initial run-down along the outer diameter of the inner electrode, as in the case of positive polarity, is not observed. In agreement with another negative DPF discharge device [24], the optimum operating pressure is found to be lower for the negative polarity case, leading to a reduction in absorption by xenon gas.

3. Experimental results

3.1. Time-dependent EUV measurements

Time-resolved measurements of the emitted in-band EUV radiation for different xenon flow rates at constant background pressure are shown in figure 5. The data were obtained with the photodiode EUV monitor described above. At low xenon concentrations a temporal shape with a single peak is observed, as with positive DPF operation. However, under conditions of a relatively low total pressure a second peak can arise at later times (ca 100 ns later) and eventually dominates the EUV emission. It coincides with the occurrence of the maximum of the discharge current. The magnitude of this second peak increases when the xenon concentration is increased. In contrast, no second EUV peak was observed for our typical operating conditions at positive polarity. From time-integrated visible imaging, there is evidence that the two peaks are separated spatially within the region viewed by the photodiode. The second peak occurs further away from the end of the cathode. Thus, the double-peaks are signatures of two successive pinch events occurring both on-axis at different distances in front of the central electrode. The intensity ratio of the two temporal peaks can be varied systematically by altering the gas mixture. It is likely that the first peak is more strongly influenced by the plasma developed on-axis due to the hollow-cathode effect, while the second peak results after a radial run-down of plasma forming in the region between the electrodes and is partly magnetically confined. The change in the ratio of the peak EUV amplitudes seems to be influenced by the discharge current density and the average gas density within the electrode region. At higher pressures the pinch time is better matched to the peak current of the drive circuit, resulting in more favourable energy coupling to the pinch plasma.

3.2. Measurements of heat removal distribution

Using a water-cooled configuration and calorimetry, we have examined the distribution of the removed heat during continuous operation at a high repetition frequency. Cooling water at up to 38 litre min^{-1} is pumped sequentially through the inner electrode, through a parallel path via four segmented cooling galleries at the outer electrode and finally through the walls of the discharge chamber and lid. At the respective inlets and outlets of each segment, thermocouple sensors monitor the water temperature. A typical result obtained for continuous operation and with negative polarity is shown in figure 6. The repetition rate is increased in steps of 250 Hz from 1000 to 2000 Hz with sufficient pausing at each interval to achieve stabilization of the water temperature. From the water temperature increase and the measured flow rate the extracted power has been calculated. The total power removed corresponded to 21 kW for the data of figure 6. Similar heat extraction experiments were carried out for operation at positive polarity. Table 1 gives a direct comparison of the heat removal at 2 kHz calculated for each section for the case of positive and negative polarity. Independent of the repetition rate, operation at negative polarity generally resulted in a smaller relative heat dissipation fraction at the inner electrode in comparison with the positive-polarity DPF.

3.3. Thermal measurements of local electrode heating in burst mode operation

In order to characterize the distribution of the thermal load on the central electrode, the black-body emission from uncooled electrodes was investigated. Using imaging with a gated ICCD camera (Andor DH520) we have observed the heating in thermal afterglow measurements for both positive and

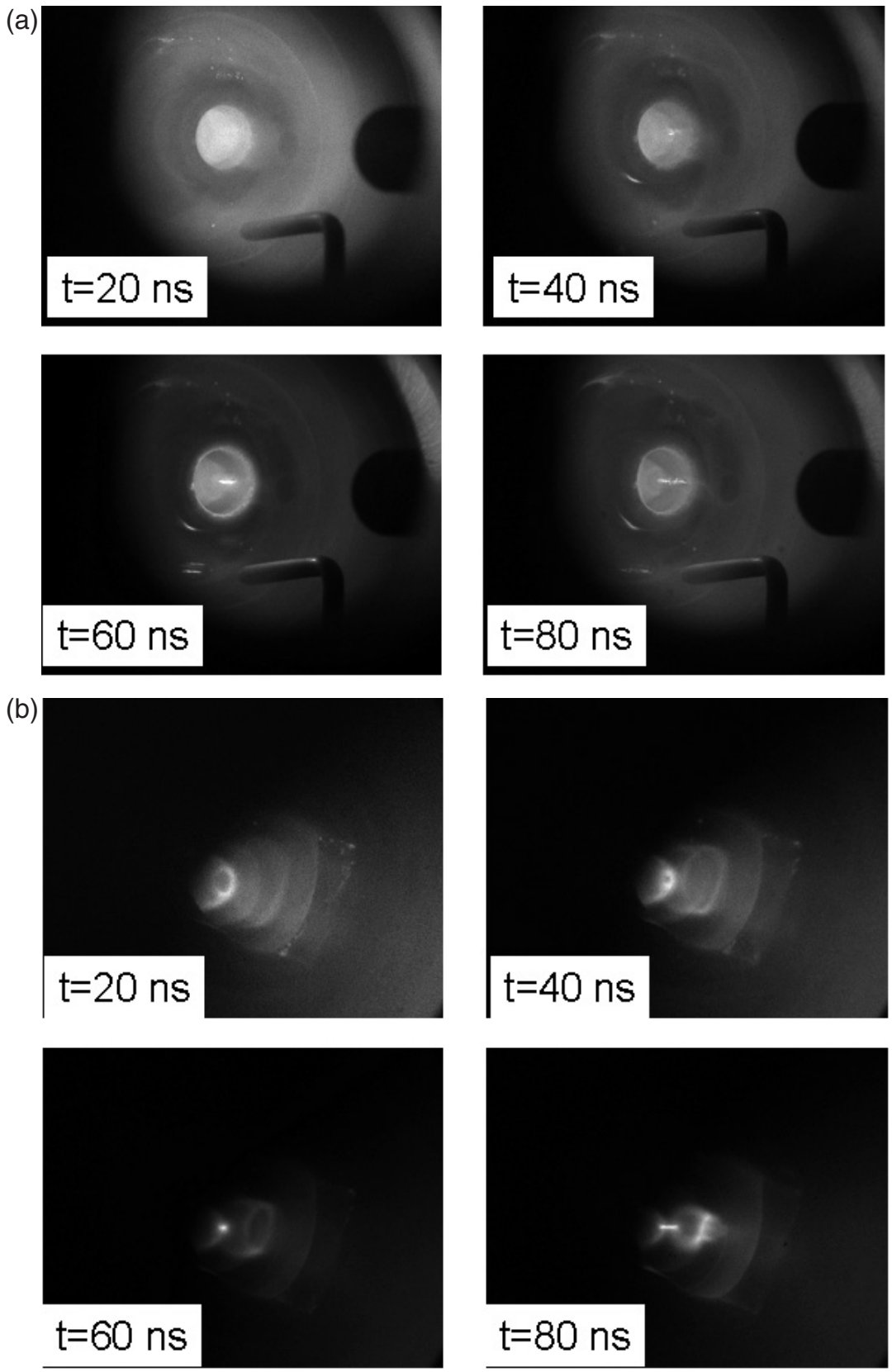

Figure 4. (*a*) Visible light images of the positive-polarity DPF during the discharge. Exposures are obtained at intervals of 20 ns using a time gate of 20 ns. At early times a plasma sheet develops, filling the region on the outside of the centre electrode. (*b*) Visible light images of the negative-polarity DPF during the initial discharge phase. Exposures are obtained at intervals of 20 ns using a time gate of 10 ns. Even early during the discharge, light emission mainly originates within the centre electrode. A circular discharge is observed during the radial implosion phase. The radial pinch phase occurs after $t = 60$ ns.

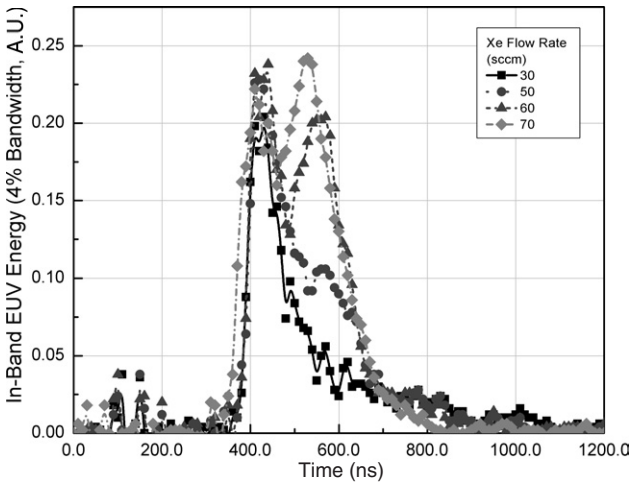

Figure 5. In-band EUV output signal as a function of time for different xenon flow rates (negative polarity configuration, single pulses). A second EUV peak that coincides with the peak current appears at higher xenon flow rates.

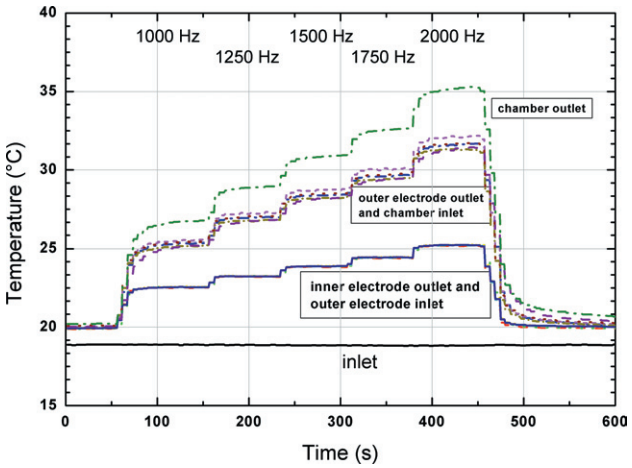

Figure 6. Water temperature profiles as detected by various temperature sensors for different DPF repetition rates. The inlet temperature sensor indicates a constant temperature of water supplied from the pump. The water temperature measured at the outlet of the inner electrode corresponds to the temperature curve recorded at the inlet of the outer electrode. Four temperature curves obtained at the outlet of the outer electrode representing the four parallel water paths are also shown. The highest temperature is recorded at the outlet of the chamber cooling line.

Table 1. Comparison of the heat removal distribution for DPF operation with positive and negative polarity.

	Positive-polarity DPF (%)	Negative-polarity DPF (%)
Inner electrode	∼50	∼35
Outer electrode	∼40	∼40
Discharge chamber	∼10	∼25

negative DPF devices operated in burst mode at 800 Hz with several hundred pulses and inter-burst times of several seconds. The camera was equipped with a 2× objective and $f = 100$ mm lens. Its spectral range (and also the sensitivity) could be changed and limited by means of a notch filter for 730 nm or by a 450 nm short-pass ultraviolet filter. The distribution of temperature versus intensity was calibrated using a direct-current heated tungsten-wire filament in a vacuum chamber. Assuming black-body radiation, the temperature of the filament is determined from its known dependence on the resistivity, as determined from the voltage and current. The same vacuum windows were used for the measurements as well as for the calibration. With the two different filters the available operating range of this thermographic imaging system was from 650°C to 2000°C. Measurements could be carried out 2–4 μs after the last pulse of a burst, subsequent to the decay of the visible light emission from the plasma.

The DPF operating conditions were optimized for highest in-band EUV. When comparing identical electrode shapes it was found that for both polarities significant heating occurs at the inner wall of the central electrode near its front end. However, for a positive-polarity DPF the central region near the exit aperture of the gas orifice is also strongly heated. Thermographic data were obtained for the hottest regions. Figure 7 shows the results of temperature decay for two regions on the anode, as indicated in the inset, for a burst length of 500 pulses. Figure 8 gives corresponding thermal afterglow data obtained with a negative DPF polarity for bursts within the range of 300–1200 pulses, averaging over four locations at the front end of the cathode. Following the initial decay the dominant cooling mechanism for the heat removal with time seems to be convective cooling by the buffer gas. This is supported by the fact that the heat deposition could be altered substantially by modifying the pressure and flow characteristics of the background gas. The highest temperature measured on the negative DPF did not exceed ∼900°C, while for positive polarity up to 1500°C was reached. This indicates that electron bombardment (positive polarity case) is inducing a much higher heat load at the central electrode compared with the ion bombardment in the negative polarity case. That is, the electron component with the plasma fluid carries most of the discharge energy.

3.4. Electrode erosion

During pulsed operation, both erosion and deposition take place at the electrodes with a net erosion loss dominating for the inner electrode. Erosion data derived from weighing of inner electrodes after exposure to several million pulses of continuous operation at ca 50 Hz are consistent with the thermal results. The weight loss per pulse due to inner electrode erosion was almost twice as high for operation at positive polarity compared with negative polarity. In both cases, burst mode operation at 1 kHz repetition rates resulted in an increase of only 50% of these typical erosion rates. As seen from a comparison of precision measurements of the inner electrode surfaces before and after several million pulses, the net electrode wear occurs primarily at the front end and in the front hollow region on the axis near the location of the xenon injection. On the other hand, erosion of the outer electrode was comparatively insignificant for both polarities.

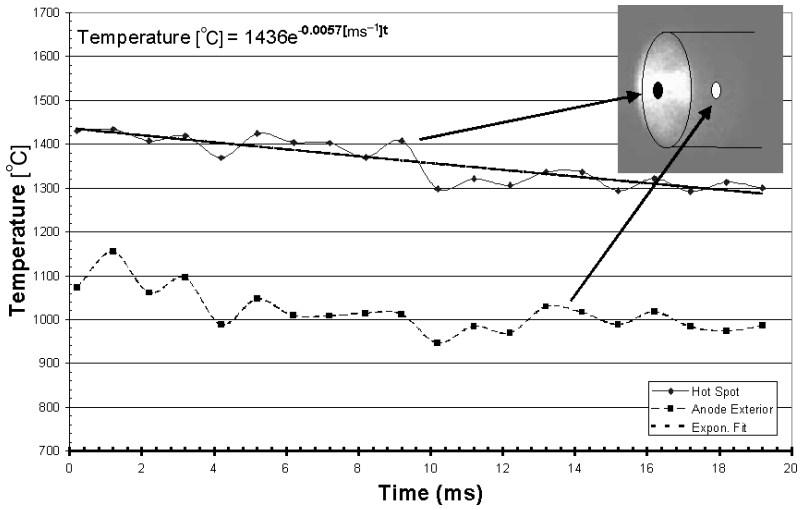

Figure 7. Temperature evolution at the inner electrode as a function of time for positive DPF operation (burst mode). Data are shown for a location at the anode exterior and for a hot spot on the interior anode wall. For this point an exponential fit is also indicated.

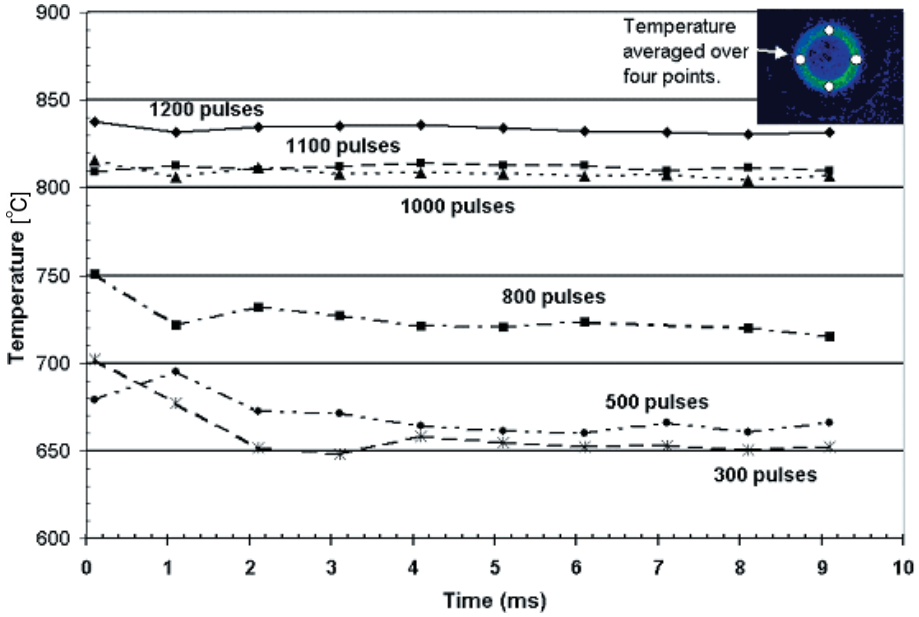

Figure 8. Temperature evolution at the inner electrode as a function of time for negative DPF operation (burst mode). Shown is the decay of the initial temperature averaged over four locations at the tip of the cathode after bursts with 300–1200 pulses.

3.5. Performance in burst mode at high repetition rates and pre-ionization

In configurations with uncooled electrodes, burst mode DPF operation at up to 5 kHz with 100 or several 100 pulses per burst was demonstrated. Generally, for burst mode operation (sequence of a fixed number of single pulses at a given frequency) the device is operated with repetitive bursts at low duty cycles of a few per cent or less. A characteristic transient occurs at the beginning of each burst. It is highly dependent on operating conditions like electrode geometry, gas mixture and pre-ionization. Figure 9 displays first single-burst results of the pulse-dependence of the in-band EUV pulse energy obtained with a positive-polarity machine at 5 kHz for different pre-ionization conditions. One type of pre-ionization scheme used a series of eight pins mounted symmetrically around the outer electrode (cathode). The pins were driven by an RF device which generated an oscillating pulse of 2–3 μs duration at about 11 MHz. Fairly high peak voltages of about 15–20 kV were applied to the pins to initiate the discharge in this configuration. The typical energy absorbed in the pre-ionization discharge was ~0.1 J. This was effective at initiating the DPF discharge, but it was difficult to cool and suffered from insulator failures due to the high peak voltages. Langmuir probe measurements of the pre-ionization discharge operated in pure xenon showed that a maximum plasma density of $\sim 5 \times 10^{13}\,\mathrm{cm}^{-3}$ was achieved near the tip of the pre-ionization pins during the time when the main pinch was triggered. The density measured at the exit of the DPF was about 50 times lower.

A second type of pre-ionization structure consisting of a $\frac{1}{4}$ wavelength copper coil driven at 145 MHz was employed at the DPF exit approximately 1 cm downstream from the end of the

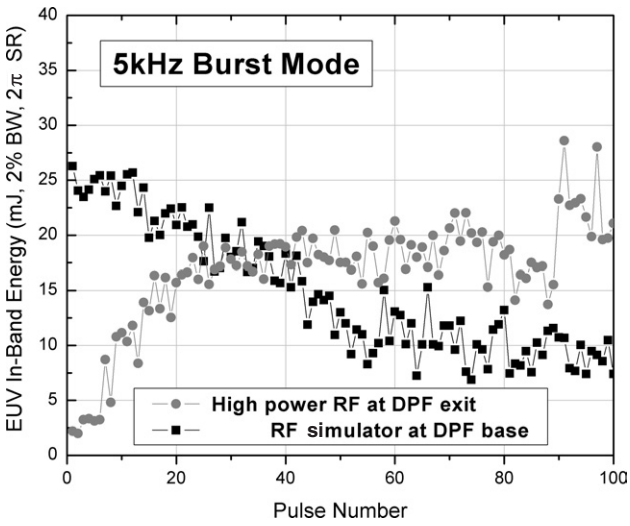

Figure 9. Results of time-integrated in-band EUV output energy in burst mode operation, positive-polarity DPF (5 kHz repetition rate). Data are shown for single bursts of 100 pulses.

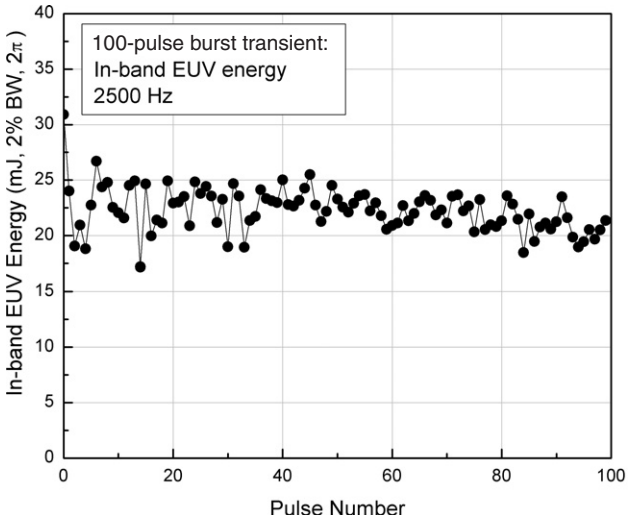

Figure 10. Results of time-integrated in-band EUV output energy in burst mode operation, negative-polarity DPF (2.5 kHz repetition rate). Data are shown for a single burst of 100 pulses.

anode electrode. This coil was driven at approximately 1 kW and was operated in pulsed mode. No probe measurements of this pre-ionization plasma were made; however, we estimate that a substantially lower plasma density was achieved at the end of the DPF electrodes based on the visible emission intensity of the plasma glow. Distinctly different behaviour was found for the initial pulses in a burst due to the variation of the location and density of the initial breakdown. The transient behaviour of the EUV pulse energy is also a strong function of the gas mixture and flow rate. Generally, for all types of pre-ionization some gas flow conditions could be found that resulted in constant energy output after an initial transient of 10–20 pulses. However, the absolute energy output depended on the gas mixture. Present testing is aimed at achieving higher pulse stability at a constant level within the burst.

Development of pre-ionization structures is aimed at minimizing the power required to achieve good pre-ionization with the electrodes located downstream of the DPF electrodes. Such configurations are desirable for high-repetition-rate operation due to the ease of cooling. For operation in positive polarity some pre-ionization was always required to initiate the first pulse. At repetition rates above ∼500 Hz we found that the required pre-ionization power could be substantially reduced. Using a negative-polarity DPF apparatus in self-breakdown mode, 100-pulse burst mode operation has been tested up to 3 kHz. Although the pulse stability was still poor (25–30% relative pulse energy fluctuation), no initial transient rise in pulse energy was observed. Results obtained in burst mode at a 2.5 kHz repetition rate are shown in figure 10.

3.6. Conversion efficiency

The EUV in-band pulse energy and the conversion efficiency as a function of input energy have already been discussed and compared previously for the two polarity cases [31]. Here, we summarize these results. EUV pulse energies of 50–60 mJ per pulse were obtained at 12–13 J deposited energy. Conversion efficiencies (conversion of energy deposited into the discharge to in-band EUV output energy) reached 0.4–0.5%. The slopes of the EUV energy and conversion efficiency versus dissipated energy curves showed a similar course for both negative and positive polarity, although the efficiency does not seem to level off as much in the negative polarity, case at the highest input energies of more than 13 J.

3.7. Source size measurements

In-band measurements of the pinch source size were carried out with a pinhole imaging system using a vacuum-compatible EUV-sensitive CCD camera (Roper Scientific, model 7471) mounted behind a pinhole (50 μm diameter), with zirconium and silicon nitride filter foils as spectral filters and attenuators. A 45° ML mirror in an arrangement similar to the EUV monitor (see figure 2) was used to eliminate out-of-band radiation. The image magnification was determined from the geometry of the arrangement. Depending on the operating conditions the averaged DPF source size has an elongated shape with a FWHM in the range of $x = 0.3$–0.4 mm and $z = 2.5$–5.0 mm, perpendicular and parallel to the axis of symmetry, respectively. A comparison of in-band measurements obtained using the EUV monitor with the integrated CCD signal has yielded almost perfect agreement on a pulse-to-pulse basis with a correlation coefficient of >0.97.

For repetition rates in the range between 2 Hz and 2 kHz a positive DPF configuration was operated with optimized gas mixtures at in-band EUV pulse energies of 45–50 mJ per pulse. The source size (FWHM) was $z = 4$–5 mm and $x = 0.3$–0.4 mm for an average of 50 pulses. Negative-polarity operation generally produced smaller source size data. For operation at in-band pulse energies in the range of 30–50 mJ per pulse the source size was $z = 3$–4 mm and $x = 0.25$–0.35 mm. A typical in-band source image for the negative polarity device is shown in figure 11.

3.8. Operation with tin as target material

In order to increase the conversion efficiency we have also tested solid target elements. Results with vaporized lithium

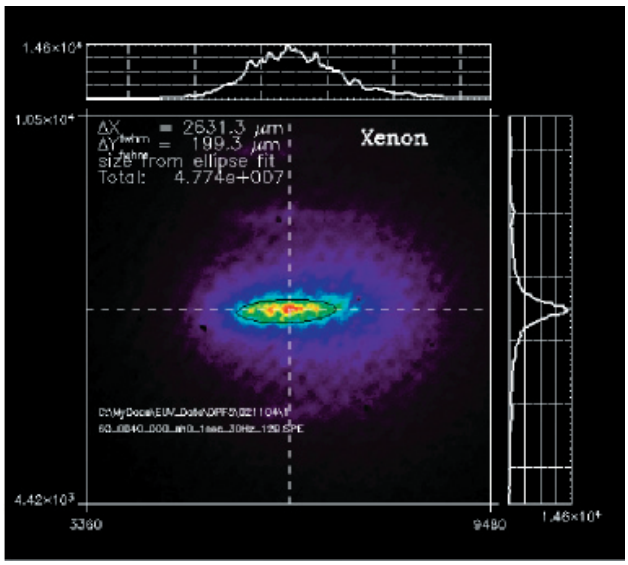

Figure 11. Source image for in-band EUV radiation obtained with a back-illuminated CCD camera. The colour code indicates the intensity of the emitted EUV radiation.

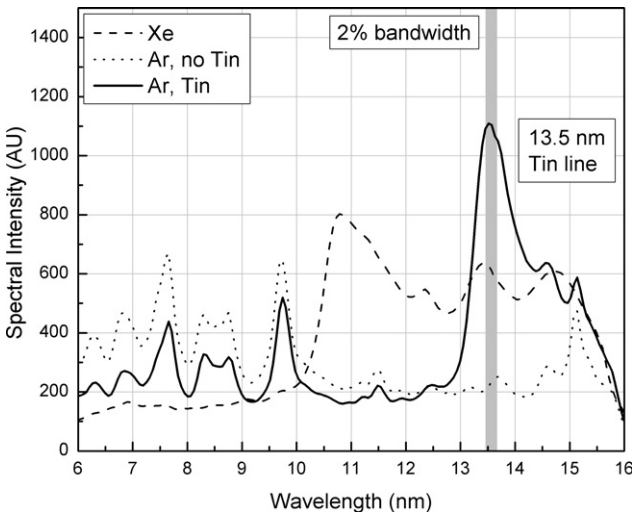

Figure 12. Transmission grating spectra for discharges with xenon, argon and argon with tin, respectively. The EUV emission is in the wavelength range from 6 to 16 nm. The 13.5 nm bandwidth region is indicated in the figure. The spectral resolution is ∼0.3 nm. The spectra are not corrected for an underlying background nearly constant with respect to wavelength.

were discussed previously [21, 22]. We have now examined tin powder targets at low repetition rate DPF operation. Using a shaker device, tin powder is immersed into argon or xenon carrier gas flowing into the discharge chamber. Micrometre- and sub-micrometre-size powder was used. The DPF with negative polarity in self-breakdown mode was employed. The waveforms obtained for argon flow and tin powder were found to be similar in shape to the curves generally obtained in this configuration (see figure 2). The EUV output energy at 13.5 nm was measured using the EUV monitor (figure 3). In order to determine the in-band emission for tin only a correction is required that takes the difference in the emission spectra into account. At optimized conditions pulse energies exceeding 200 mJ per pulse were recorded. At the highest energies deposited in the discharge we have measured up to 1.6% conversion efficiency. Using a transmission grating arrangement described previously [32], low-resolution EUV emission spectra were recorded in the wavelength range from 6 to 16 nm. Figure 12 shows a comparison of spectra obtained with argon gas, with argon in combination with tin powder and with xenon gas. Argon exhibits mainly transitions that lie far outside the 13.5 nm band. However, with the addition of tin, strong emission centred near 13.5 nm is observed. Compared with the Xe spectrum, a significant reduction of out-of-band radiation is observed in addition to the higher spectral EUV intensity near 13.5 nm. Source-size measurements were also carried out for this configuration (see figure 13). Compared with xenon the argon/tin mixture showed a less elongated and more spherical emission volume of the pinch region. For Sn/Ar typical source size values were in the range of $x = 0.6$–0.8 mm and $z = 2.0$–3.0 mm.

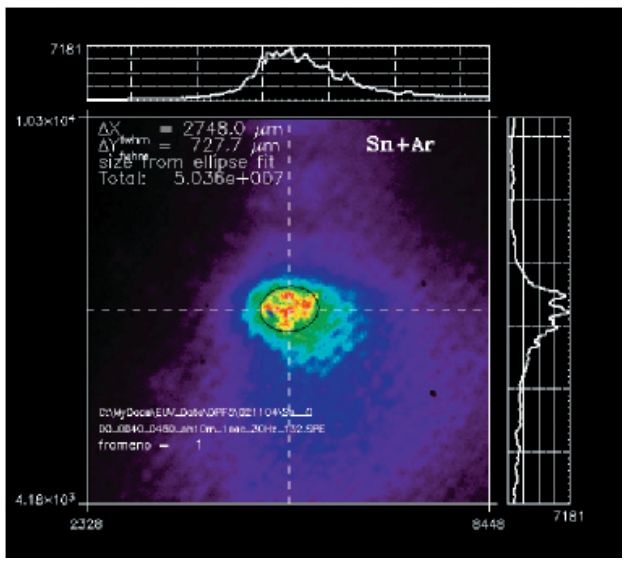

Figure 13. In-band image of the EUV radiation emitted from the negative-polarity DPF pinch discharge for the case of tin. Compared with figure 11 the aspect ratio (length to diameter) is lower.

4. Discussion and comparison

Operation of the DPF configuration with different polarity of the inner electrodes showed very different plasma dynamics at times before the final pinch compression phase. The positive DPF exhibits the conventional behaviour where a rundown phase in the annular region between the electrode precedes the radial pinch compression phase. The negative DPF is characterized by a self-pre-ionizing hollow-cathode initiation phase that occurs on the axis inside of the inner electrode prior to the pinch compression. The negative polarity configuration is advantageous in that the ions that move towards the cathode have the appropriate general direction of their momentum (radially inwards) at the time of pinch compression, whereas the pinch compression has to work against the initial ion momentum in the other polarity case.

Another important factor is the influence of electron bombardment, since it is directly related to electrode heating

and erosion. In the DPF configuration the current density is highest at the front edges and inner surface of the inner electrode. During operation the highest plasma–wall heating occurs in these regions. Electrode erosion by evaporation and micro-melting with subsequent splashing is most severe at these locations, as is also seen by the observed erosion pattern. Comparison of our results for the two polarities indicates that electron bombardment is significantly more effective in generating electrode erosion than ion sputtering. The calorimetric data for heat removal, the thermographic afterglow data as well as the inner electrode erosion pattern and erosion amount point towards more favourable operating conditions for a negative-polarity DPF with respect to heating of the inner electrode. In this configuration the power dissipation at the inner electrode is reduced at the expense of more plasma–wall heating in the discharge vessel. Since most of the electrode erosion occurs at the inner electrode, during operation at high powers and high continuous repetition rates also, the reversed-polarity configuration leads to significantly reduced generation of debris.

Other advantages of negative-polarity DPF machines are the observation of a smaller source size at comparable conditions and an operation mode at a generally lower xenon density. Energy coupling is generally improved at low Xe flow. This leads to a reduction of EUV absorption by the xenon background gas. The source size is typically smaller and has a more spherical shape for the DPF with negative polarity. This holds in particular for operation with tin as the metal target element. A smaller etendue of the source is very advantageous since it translates directly into higher collectable EUV output [34].

The pulse-to-pulse stability and the general evolution of the EUV pulse energy within a burst at high repetition rates depend very sensitively on the operating and pre-ionization conditions. The influence of pre-ionization is largely connected to the development of the initial discharge behaviour prior to the pinch and its influence on the coupling of the electrical energy into the discharge medium. This can be deduced from the different pulse-to-pulse behaviour for pre-ionization with different intensities and different spatial extent. The initial transient course seems to be connected with heating of the electrodes, and convective cooling by the surrounding gas is likely a contributing mechanism for the observed changes during the first few pulses in the burst.

5. Conclusions

The presented data demonstrate that the intense short-pulse plasma focus EUV radiation source studied here can generally be operated with similar output energies and conversion efficiencies for both positive and negative charging polarity. However, for future use and integration in demanding lithography manufacturing applications a radiation source operated at negative polarity provides several distinct advantages: efficient discharge initiation can be obtained in a self-breakdown mode. Generally, the xenon operating pressure is lower, leading to reduced absorption of the generated EUV radiation. The relative heat load deposited at the inner electrode that is most difficult to cool is smaller. In addition to the thermal heating there is evidence that the electrode erosion is also less severe. Generally, and especially when using tin powder as a target element, the source size is also smaller. However, the stability and electrode lifetime continue to be challenges for providing manageable source performance in an operating regime at continuous repetition rates beyond 3 kHz.

Acknowledgments

We would like to thank all members of the EUV development team at Cymer for their invaluable support. We also acknowledge the continuous help of our product development group. We would like to acknowledge Cooke Corp. for the use of their high-speed framing camera in our studies. This work was supported in part by DARPA contract N66001-03-C-8017.

References

[1] Filippov N V, Filippova T I and Vinogradov V P 1962 *Nucl. Fusion* (Suppl. **2**) p 577
[2] Mather J W 1971 *Methods of Experimental Physics, Plasma Physics* vol 9B, ed H R Griem and R H Loveberg (New York: Academic) p 187
[3] Krompholz H, Rühl F, Schneider W, Schönbach K and Herziger G 1981 *Phys. Lett.* A **82** 82
[4] Zakaullah M, Ahmad I, Omar A, Murtaza G and Beg M M 1996 *Plasma Sources Sci. Technol.* **5** 544
[5] Zakaullah M, Akhtar I, Waheed A, Alamgir K, Shah A Z and Murtaza G 1998 *Plasma Sources Sci. Technol.* **7** 206
[6] Serban A and Lee S 1997 *Plasma Sources Sci. Technol.* **6** 78
[7] Beg F N, Ross I, Lorenz A, Worley J F, Dangor A E and Haines M G 2000 *J. Appl. Phys.* **88** 3225
[8] Silva P, Soto L, Moreno J, Sylvester G, Zambra M, Altamirano L, Bruzzone H, Clausse A and Moreno C 2002 *Rev. Sci. Instrum.* **73** 2583
[9] Moreno J, Silva P and Soto L 2003 *Plasma Sources Sci. Technol.* **12** 39
[10] Neff W, Eberle J, Holz R, Lebert R and Richter F 1989 *SPIE* **1140** 13
[11] Bergmann K and Lebert R 1995 *J. Phys. D: Appl. Phys.* **28** 1579
[12] Lebert R, Rothweiler D, Engel A, Bergmann K and Neff W 1996 *Opt. Quant. Electron.* **28** 241
[13] Lee S, Lee P, Zhang G, Feng X, Gribkov V A, Liu M, Serban A and Wong T 1998 *IEEE Trans. Plasma Sci.* **26** 1119
[14] Gribkov V A, Mahe L, Lee P, Lee S and Srivastava A 2000 *Proc. SPIE* **4226** 151
[15] Petr R, Reilly D, Freshman J, Orozco N, Pham D, Ngo L and Mangano J 2000 *Rev. Sci. Instrum.* **71** 1360
[16] Mayo R M, Bourham M A, Glover M E, Caress R W, Earnhart J R D and Black D C 1995 *Plasma Sources Sci. Technol.* **4** 47
[17] Scheuer J T, Schoenberg K F, Gerwin R A, Hoyt R P, Henins I, Black D C, Mayo R M and Moses R W Jr 1994 *IEEE Trans. Plasma Sci.* **22** 1015
[18] Ziemer J, Cubbin E, Choueiri E and Birx D 1997 Performance characterization of a high efficiency gas-fed pulsed plasma thruster *33rd AIAA/ASME/SAE/ASEE Joint Propulsion Conf. (Seattle)* AIAA-97-2925 http://alfren.princeton.edu/papers/JKZSRLJPC97abstext.htm
[19] Birx D 1999 Plasma gun and methods for the use thereof *US Patent* 5,866,871
[20] Ziemer J K and Choueiri E Y 2001 *Plasma Sources Sci. Technol.* **10** 395
[21] Partlo W, Fomenkov I and Birx D 1999 *Proc. SPIE* **3676** 846
[22] Partlo W, Fomenkov I, Oliver R and Birx D 2000 *Proc. SPIE* **3997** 136
[23] Decker G, Kies W and Pross G 1982 *Phys. Lett.* A **89** 393

[24] Kato Y, Ochiai I, Watanabe Y and Murayama S 1988 *J. Vac. Soc. Technol.* B **6** 195
[25] Kato Y 1994 *Japan. J. Appl. Phys.* **33** 4742
[26] Mathuthu M, Zengeni T G and Gholap A V 1997 *Rev. Sci. Instrum.* **68** 1429
[27] Mathuthu M, Zengeni T G and Gholap A V 1998 *IEEE Trans. Plasma Sci.* **26** 14
[28] Partlo W N, Fomenkov I V, Ness R M, Oliver R I, Melnychuk S T and Rauch J E 2001 *SPIE* **4343** 232–48
[29] Fomenkov I V, Partlo W N, Ness R M, Oliver R I, Melnychuk S T, Khodykin O V and Böwering N R 2002 *SPIE* **4688** 634–47
[30] Fomenkov I V, Ness R M, Oliver I R, Melnychuk S T, Khodykin O V, Böwering N R, Rettig C L and Hoffman J R 2003 *SPIE* **5037** 807–21
[31] Fomenkov I V, Ness R M, Oliver I R, Melnychuk S T, Khodykin O V, Böwering N R, Rettig C L and Hoffman J R 2004 *SPIE* **5374** 168–82
[32] Böwering N, Martins M, Partlo W N and Fomenkov I V 2004 *J. Appl. Phys.* **95** 16–23
[33] Pankert J, Bergmann K, Klein J, Neff W, Rosier O, Seiwert S, Smith C, Apetz R, Jonkers J, Loeken M and Derra G 2002 *SPIE* **4688** 87–93
[34] Derra G and Singer W 2003 *SPIE* **5037** 728–41